Dynamic Analysis of Small Wind Turbines Frequency Support Capability in a Low-Power Wind-Diesel Microgrid

Raffael Engleitner, Ademir Nied, Mariana Santos Matos Cavalca, and Jean Patric da Costa

***Abstract*—When wind power accounts for a large portion of the islanded microgrid power, it may need to support the ac bus frequency regulation. The increasing penetration of variable speed wind turbines (WTs) in microgrids leads to a lower inertia, as the rotational speed of the turbine and the grid is decoupled by power electronic converters. Lower system inertia results in a larger and faster frequency deviation after occurrence of abrupt variations on generation and load. It is possible to implement control loops in the WT converters to provide a virtual inertia and support frequency regulation in the microgrid. This paper investigates the variables related to the frequency compensation capability of WT, such as kinetic energy, dc-link capacitance, turbine size, wind penetration, number of turbines, operating region along the power curve, power reserve and droop control gain, etc. The analysis is structured as a design of experiment (DOE) to have a clear and organized comparison of multiple system configurations. An optimal control technique is applied to provide fair comparison among the system variables. A flowchart explaining how the DOE and controllers gains were defined is provided.**

***Index Terms*—DC-link voltage control, design of experiment (DOE), frequency support, isolated microgrids, linear quadratic regulator (LQR), permanent-magnet generator, wind penetration, wind power generation.**

I. Introduction

THE USAGE of distributed generation (DG) units has grown considerably in recent times. As a way to decentralize the electricity generation and transmission, this strategy provides lower transmission losses and generation redundancy, among other benefits [1]. On the other hand, it may insert intrinsic challenges into system reliability and operation [1], [2].

In order to overtake grid-connection issues, the generation units and the associated loads have been approached as subsystems of the main grid, commonly called as microgrids [1]. These microgrids normally contain energy storage systems (ESSs), traditional generators, and renewable energy sources (fuel-cell, photovoltaic, ocean energy, biogas digesters, microturbines, wind systems, etc.), operating in a controllable system, able to provide reliable energy to a local area [1], [2].

A microgrid can operate basically in grid-connected mode or islanded mode. In the first operation mode, it follows the grid voltage and frequency references to inject reactive and active power following maximum power point tracking (MPPT) algorithms or dispatched references. In the second operation mode, the DG units are responsible for controlling the frequency and voltage of the ac bus as well as sharing the total load demand according to their power rating [3].

In islanded microgrids, parallel DG systems have been commonly controlled by the voltage and frequency droop control technique and similar strategies [4]–[6]. However, there is an inherent challenge in the frequency control when most renewable sources are connected to the grid via static power converters, providing different inertia behavior than conventional generators [6], [7]. Some sources own none rotating parts, like photovoltaic cells and fuel cells, having no direct relationship to the grid inertia. Other sources may be constituted by rotating masses, for instance, wind turbines (WT) and microturbines. Nevertheless, in most cases, they are driven by power converters, not proving direct relationship to the inertia.

Traditionally, remote microgrids have been supplied by diesel or gas units connected to synchronous generators (SG) as the main energy source, due to the reliability and confidence in this technology [10], [11]. On the other hand, they have seen an increased penetration of renewable generation in recent times, driven mainly by social pressures related to environmental awareness and economical strategies intending to diversify the nature of energy sources [12], [13]. The increased penetration may deteriorate the overall microgrid inertia, providing a high rate of system frequency deviation during transient periods [7], [13]. This issue becomes even more critical as the microgrid total power becomes lower, what occurs in small rural communities, industrial sites, commercial buildings or house communities. For these cases, each load tends to drain a big portion of the total power, providing higher transients [14].

The small wind turbine (SWT)-based DG units are one of the fastest growing sources of power generation, mainly due to resources availability, rapid technological development, and low landscape impact [15], [16]. Most SWTs adopt permanent

Manuscript received June 4, 2017; revised August 25, 2017; accepted September 4, 2017. Date of publication October 9, 2017; date of current version January 18, 2018. Paper 2017-PSEC-0576.R1, presented at the 2016 IEEE International Conference on Industry Applications, Curitiba, Brazil, Nov. 20–23, and approved for publication in the IEEE TRANSACTIONS ON INDUSTRY APPLICATIONS by the Power System Engineering Committee of the IEEE Industry Applications Society. *(Corresponding author: Raffael Engleitner.)*

R. Engleitner, A. Nied, and M. S. M. Cavalca are with the State University of Santa Catarina, Joinville, SC CEP 89223-100, Brazil (e-mail: rengleitner@gmail.com; ademir.nied@udesc.br; mariana.cavalca@udesc.br).

J. P. da Costa is with the Electrical Engineering Department, Federal Technological University of Parana, Pato Branco, PR CEP 85503-390, Brazil (e-mail: jpcosta@utfpr.edu.br).

Color versions of one or more of the figures in this paper are available online at http://ieeexplore.ieee.org.

Digital Object Identifier 10.1109/TIA.2017.2761833

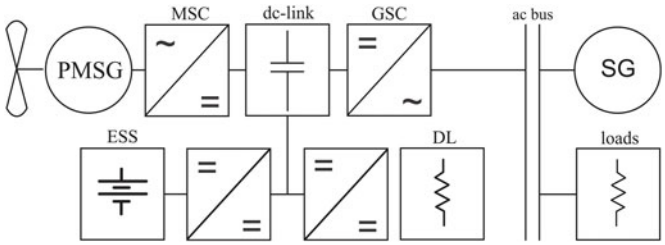

Fig. 1. Traditional diesel and SWT-based microgrid structure.

magnet synchronous generators (PMSG) due to its higher power density, better controllability, and higher number of pole pairs, avoiding gearboxes. This generator technology is normally driven by a full power converter which decouples the machine from the grid, allowing flexible speed control strategies and avoiding active pitch control devices [16]–[18]. SWT-based applications tend to spread worldwide, encouraged by grid codes and national laws imposing simpler grid connection and higher feed-in tariffs [15]–[18].

Although the aforementioned scenario highlights the importance of the frequency support from the SWT side in low-power microgrids, most references focus on higher power systems [19]–[25]. These references show that the nonlinearity of the turbine model, the intermittency of the wind, and the slow time constant of the rotors provide an interesting challenge from the control point of view. Therefore, their focus is more related to system stability than to dynamic response itself, what is acceptable for higher power systems where the each load drains a lower part of the total available power, providing lower transients [14].

A conventional islanded PMSG-based microgrid is presented in Fig. 1. It is provided of a dump load (DL) as a matter of dc-link overvoltage protection and an ESS due to the wind intermittency [16], [26]–[30]. There is a machine-side converter (MSC) that controls the generator speed and a grid-side converter (GSC) which controls the energy exchange between the grid and the dc link. The grid is usually connected to a synchronous machine as either the main or the secondary energy source [10], [11], [16]. Considering the presence of wind, the operation modes for this system are basically four: wind and SG mode (WSG); wind only mode (WO), and the two derivatives with ESS support.

In the WSG mode, the GSC compensates the ac-bus frequency deviations while the MSC controls the dc-link through WT speed control. As mentioned previously, this task has been hard when the power of the microgrid is low. In the WO mode, the GSC works as a grid-forming device, requiring even higher active energy management performance. So far, this performance has not been delivered from the WT itself due to the dynamics and the intermittency involved, so the literature proposes basically two solutions.

1) To use an ESS with a bidirectional converter to drain or source energy from the dc link to complement the difference between load and the generation [26]–[30]. This solution is fast in terms of response, but stresses the ESS due to the consecutive charges and discharges, adding cost associated to maintenance. Besides, the ESS may not be available all the time as it could be either full, empty or not operational, requiring another microgrid operation mode.
2) To drive the generator in MPPT mode and burn the energy excess through a DL [29], [31]. The DL is the fastest device to limit the energy sourced, but has no energy margin for positive load transients, limiting this application.

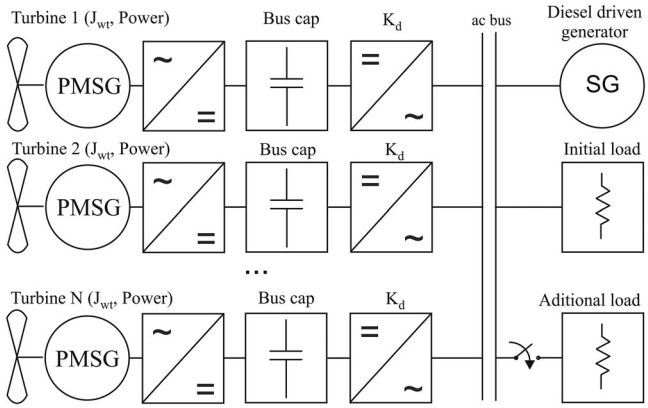

Fig. 2. Simulated microgrid.

From all the operating modes above, the most challenging ones are WO and WSG with the turbine itself providing the required active power for frequency transients. Therefore, many references have studied these operating modes in the literature, for instance [32]–[39]. An interesting analysis was done by Yuan *et al.* [39], where a hybrid adaptive PI controller was implemented to limit the mechanical losses along speed transients. The author also commented about operating the WT in the left or right side of the power curves, called as Sector I (left) and Sector II (right), but there was no clear comparison or conclusion about the benefits or detriments for each operating sector as well as the relationship between sector and other system variables.

In general, the literature has considered a limited number of system parameters to be analyzed concomitantly. This simplification does not provide a clear and overall understanding of the system interactions.

Considering such context, the purpose of this work is to investigate how fast the system may respond and what is the impact of each parameter related to the frequency compensation capability of SWT. The objective is to analyze concomitantly a higher number of system variables, such as WT size, wind penetration, power reserve (deloading), operating sectors (I or II), dc-link capacitance and GSC droop constant. As there are many parameters to be evaluated, the analysis was done through the simulation environment, structured in a design of experiment (DOE) pattern with a clear exposition of the results and impact of those variables [40]. The variables mentioned were swept following a two-level factorial experiment structure while other parameters were kept constant along the simulations.

The simulated microgrid is driven mainly by a SG able to provide 8.1 kVA at 400 Vrms L-L and 50 Hz, which is controlled by a diesel engine with two PI-based loops for frequency and voltage regulation. As can be seen in Fig. 2, there is a SWT-based system to support the power generation and frequency regulation of the ac bus through GSC droop control. The dynamic analysis

is done at a transient driven by an additional load connection into the ac bus while the system is operating in a WSG mode. The additional load represents the connection of a customer load into the ac bus.

A linear quadratic regulator (LQR) is proposed to obtain the optimum control trajectory in terms of bus voltage compensation and provide fair comparison between different system variables, once it keeps the relationship among states and control energy for fixed weight matrices. Moreover, it can easily recalculate the control gains according to different system parameters, not having any kind of human interference or empirical equations as part of the tuning process.

II. SWT System Modeling

The power generated from a WT depends on the site-specific wind speed, which fluctuates randomly with time [41]. The rotor aerodynamics of a WT is represented by the well-known static relationship

$$P_{\rm ex} = 0.5\rho A C_p {v_w}^3 \tag{1}$$

where $P_{\rm ex}$ is the power extracted from the wind in watts, ρ is the air density in kg/m³, C_p is the power coefficient, v_w is the wind speed upstream of the rotor in m/s, and *A* is the area swept by the rotor in m² ($A = \pi R^2$), being *R* the radius of the blades in meters [41]. For notation simplification purposes, the term (*t*) is suppressed.

The amount of aerodynamic torque (T_w) in N·m is given by

$$T_w = P_{\rm ex}/\omega_r \tag{2}$$

which is the ratio between the power extracted from the wind and the rotor speed (ω_r) in rad/s [41]. It should be noted that the mechanical torque transmitted to the generator ($T_{\rm wg}$) is the same as the aerodynamic torque, since there is no gearbox considered in this work. The equation defining the power coefficient as a function of the tip-speed ratio and the blade pitch angle is defined as follows:

$$C_p(\lambda,\theta) = c_1\left(c_2\left(\frac{1}{\beta}\right) - c_3\theta - c_4\theta^x - c_5\right)e^{-c_6\frac{1}{\beta}}. \tag{3}$$

Since this function depends on the WT rotor type, the coefficients $c_1 - c_6$ and *x* can be different for various turbines. Additionally, the parameter β is also defined in different ways according to [41], for example

$$\frac{1}{\beta} = \frac{1}{\lambda + 0.08\theta} - \frac{0.035}{1+\theta^3} \tag{4}$$

where θ is the pitch angle in degrees, and the tip-speed ratio λ is defined as follows:

$$\lambda = \omega_r R/v_w. \tag{5}$$

The parameters of the turbines considered in this work are taken from [41], which are $c_1 = 0.5$, $c_2 = 116$, $c_3 = 0.4$, $c_4 = 0, c_5 = 5, c_6 = 21$, *x* is not used, $\rho = 1.205$ kg/m³, rated wind speed $(v_w) = 12$ m/s, and maximum power coefficient $C_p = 0.4412$. The pitch angle is 0 as no active pitch control is implemented.

The drive train of a SWT generator system consists normally of a hub with blades, a rotor shaft and a gearbox with breaker and generator. For the purpose of the present research, neither viscosity nor damping effects have been considered in the drive. According to [42], the blades provide much higher inertia than the generator itself and the equivalent moment of inertia of the WT (J_{wt}) in kg·m² can be approximated by the empirical equation

$$J_{\rm wt} = 1.74 \cdot 10^{-7} P_{\rm nom}^{2.13} \tag{6}$$

where $P_{\rm nom}$ is the rated power of the turbine in watts. The equation that describes the generator rotor angular speed is

$$\frac{d\omega_r}{dt} = \frac{T_{\rm wg} - T_e}{J_{\rm wt}} - \frac{b_{\rm wt}}{J_{\rm wt}}\omega_r \tag{7}$$

where $b_{\rm wt}$ is the equivalent damping coefficient in N·m/rad/s and T_e is the generator electrical toque in N·m.

The dynamic model of the PMSG is derived from the two-phase synchronous reference frame, which the *q*-axis is 90° ahead of the *d*-axis with respect to the direction of rotation [43]. The dq0 model of a PMSG with *d*-axis aligned to the rotor frame can be described as follows:

$$\dot{i_{sd}} = -\frac{R_s}{L_d}i_{sd} - N_{\rm pp}\frac{L_q}{L_d}\omega_r i_{sq} - \frac{1}{L_d}v_{sd} \tag{8}$$

$$\dot{i_{sq}} = -\frac{R_s}{L_q}i_{sq} + N_{\rm pp}\frac{L_d}{L_q}\omega_r i_{sd} + N_{\rm pp}\frac{K_m}{L_d}\omega_r - \frac{1}{L_q}v_{sq} \tag{9}$$

where K_m is the permanent magnetic flux in Wb, $N_{\rm pp}$ is the number of poles pairs of the generator, R_s is the phase resistance, L_d and L_q are the direct and quadrature axis inductances, respectively, while i_{sd} and i_{sq} are the respective stator currents and v_{ds} and v_{qs} are the stator voltages.

The relationship between rotor speed and electrical speed (ω_e [rad/s]) is

$$\omega_e = N_{pp}\omega_r. \tag{10}$$

The electromagnetic torque, the mechanical speed, and rotor position are given by

$$T_e = 1.5N_{\rm pp}\left[\left(L_d - L_q\right)i_{sd} + K_m\right]i_{sq} \tag{11}$$

$$\dot{\omega_r} = -\frac{b_{\rm wt}}{J_{\rm wt}}\omega_r + \frac{T_{\rm wg} - T_e}{J_{\rm wt}} \text{ and } \dot{\theta_r} = \omega_r. \tag{12}$$

The power generated is the same as the extracted wind power ($P_{\rm ex}$) in steady state neglecting the MSC losses [39]. During speed transients, the required mechanical power for acceleration or deceleration is

$$\omega_r J_{\rm wt}\frac{d\omega_r}{dt} - {\omega_r}^2\frac{b_{\rm wt}}{J_{\rm wt}} = P_{\rm ex} - P_g. \tag{13}$$

Neglecting the converter losses, according to [39], the dc-link voltage dynamic equation can be written as

$$P_g - P_{\rm load} = v_{\rm dc}i_c = v_{\rm dc}C_b\frac{dv_{\rm dc}}{dt} \tag{14}$$

where $v_{\rm dc}$ and i_c are the voltage and current of the dc-link capacitor, respectively, $P_{\rm load}$ is the power drained by the GSC,

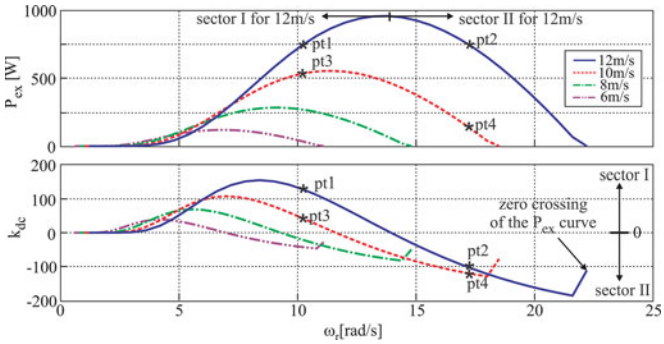

Fig. 3. Power ratio characteristics of the turbine for different wind speeds and pitch angle fixed at 0°.

TABLE I
PMSG PARAMETERS

Parameter	T_1	T_2	T_3	Unit
Line peak voltage	440	440	440	V
Nominal speed	13.8	9.2	6.9	rad/s
Generator poles pairs ($N_{\rm pp}$)	21	21	21	–
Stack width	7.2	7.2	7.2	mm
Stack height	41.2	61.8	82.4	mm
Stator resistance (R_s)	4.48	2.30	1.17	Ω
Wire diameter	1	1.7	2.9	p.u.
Stator inductances (L_d, L_q)	54.8	82.2	109.6	mH
Torque constant (K_t)	7.82	11.73	15.64	N·m/A
Flux linkage constant (K_m)	0.201	0.301	0.402	V.s
Moment of inertial ($J_{\rm wt}$)	0.383	1.676	7.33	Kg·m²
Friction factor ($b_{\rm wt}$)	0.0057	0.0249	0.109	N·m·s

and P_g is the generated power given by

$$P_g = \omega_r T_e. \tag{15}$$

Substituting (13) and (1) into (14) returns

$$\frac{1}{2}\rho A c_p {v_w}^3 - P_{\rm load} - v_{\rm dc} C_b \frac{dv_{\rm dc}}{dt} = J_{\rm wt}\omega_r \frac{d\omega_r}{dt} - \frac{b_{\rm wt}}{J_{\rm wt}}{\omega_r}^2 \tag{16}$$

which represents the nonlinear relationship between the dc-link voltage and PMSG speed [39]. Neglecting friction losses and obtaining the linear model of (16) trough perturbation and linearization at a given operating point (e.g., dc-link voltage $\bar{v}_{\rm dc}$, PMSG speed $\bar{\omega}_r$, and wind speed $\bar{v}_w$) results in the transfer function of the dc-link voltage by the shaft speed as

$$\frac{v_{\rm dc}(s)}{\omega_r(s)} = \frac{\bar{k}_{\rm dc} - J_{\rm eq}\bar{\omega}_r s}{sC_b\bar{v}_{\rm dc}} \tag{17}$$

where $\bar{k}_{\rm dc}$ is the derivative of the wind power curve (1) by the speed at an operating point [39].

In order to detail further the behavior of the turbine described by (16) and (17), both wind power and $k_{\rm dc}$ curves are plotted in Fig. 3 for different wind speeds, considering an actual PMSG detailed in Table I. The curves reveal that for a given power level, there can be two possible operating points (e.g., pt1 and pt2) and for a given shaft speed coexists multiple power levels due to different wind speeds (e.g., pt1 and pt3).

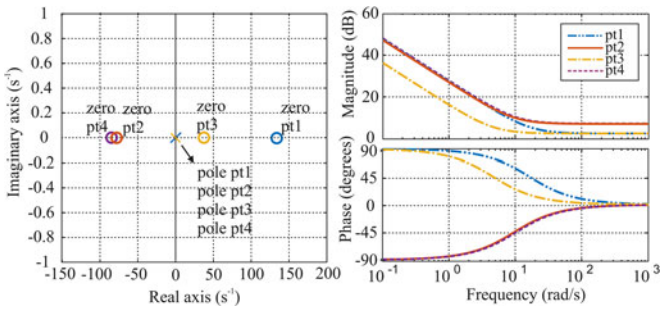

Fig. 4. Root locus and frequency response for different operating points.

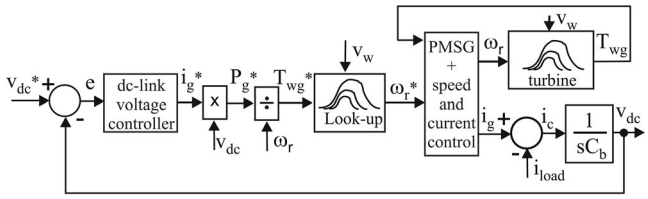

Fig. 5. DC-link voltage control block diagram.

The transfer function (17) has different dc gains, poles and zeros according to the operating points as illustrated in Fig. 4 for the same operating points from Fig. 3. As can be observed, the positive slope side (Sector I) has a right half-plane zero (RHZ), providing a nonminimum phase behavior. Whenever an under voltage occurs in Sector I, the system accelerates to extract more power; however, part of the energy is turned into kinetic energy, going against the control. As the speed is lower, the mechanical losses are lower as well.

For overvoltage in Sector I, the system needs to be slowed down, part of the kinetic energy turns into electrical energy, increasing the voltage bus. The opposite occurs for the negative slope curve (Sector II), where there is a left half-plane zero and the kinetic energy works in favor to the control action (minimum phase behavior).

Equations (13)–(17) have been simplified in order to obtain a general system model and understand the overall behavior. The control design and the simulations, on the other hand, consider detailed models for each system block.

III. CONTROL DESIGN

The concepts of the control have been developed in [45] and in the present paper new theoretical evidences that confirm the previous analysis were included.

The block diagram for the control system is shown in Fig. 5. The dc-link voltage control loop generates the required PMSG speed reference (ω_r^*). The output of the dc-link compensator generates the current reference, which is treated to generate a toque reference. The turbine model is saved into a lookup table which considers the wind speed and the turbine torque as input while ω_r^* comes in its output. The bus voltage loop considers the blocks from i_g^* to i_g as unity gain. This assumption is valid once this inner system (machine speed and currents loops) works around ten times faster than the voltage loop dynamics. The generator control follows the speed reference threating

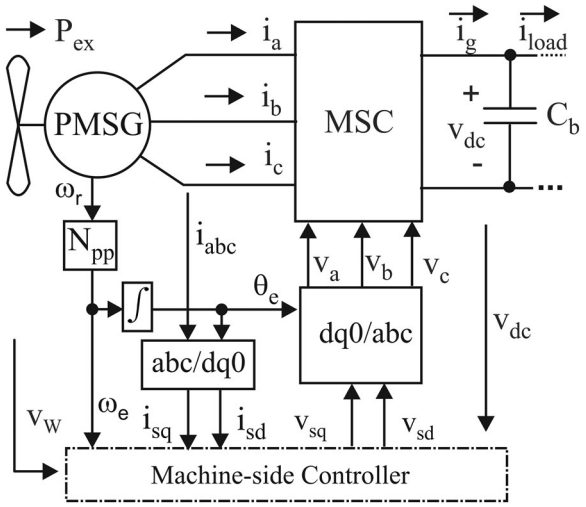

Fig. 6. FOC control applied to the PMSG.

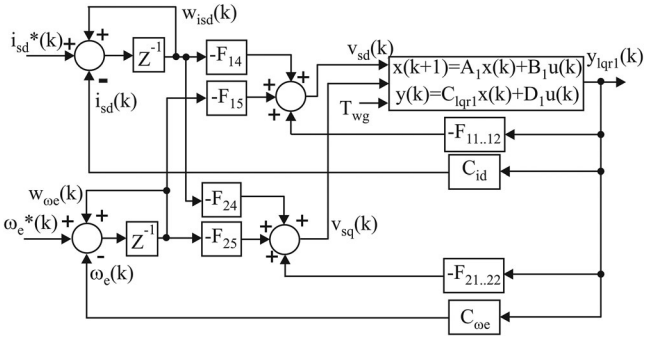

Fig. 7. LQI applied to PMSG speed and current control.

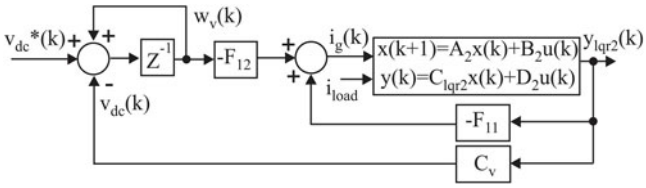

Fig. 8. LQI applied to dc-link voltage control.

the turbine torque ($T_{\rm wg}$) as a disturbance. The resulting current (i_g) from the generator inverter feeds and regulates the dc-link voltage.

The generator speed and current control loops are implemented through field-oriented control (FOC) in the dq0 synchronous reference frame according to Fig. 6.

In order to design the control, the PMSG behavior defined previously by (8), (9), and (12) is described as a linear time-invariant discrete-time system in the form

$$x(k+1) = Ax(k) + Bu(k), y(k) = Cx(k) + Du(k) \quad (18)$$

where $x(k)\,\epsilon\,R^n$, $u(k)\,\epsilon\,R^m$, and $y(k)\,\epsilon\,R^q$ are the states, inputs and outputs vectors defined as follows:

$$x(k) = y(k) = \left[\, i_{sd}\,(k) \quad i_{sd}\,(k) \quad \omega_e\,(k) \,\right]^T \quad (19)$$

$$u(k) = \left[\, v_{sd}(k) \quad v_{sq}(k) \quad T_{\rm wg}(k) \,\right]^T. \quad (20)$$

According to [46] for the LQR, assuming that the system (18) with $x(0) = x_0$ is stabilizable, there is a control law defined by *u(k) = –Fx(k)* that minimizes the cost function

$$J = \sum_{k=0}^{\infty} \left(x^T\,(k)\, Qx\,(k) + u^T\, Ru\,(k) \right) \quad (21)$$

with *Q* and *R* as matrices that ponder the energy of the states and control action, respectively. Both matrices are real and symmetric, being *Q* semidefined and *R* defined. The linear-quadratic-integral controller (LQI) is based on the LQR with the addition of one or more integrators in order to turn it into reference tracker. For the FOC structure presented in Fig. 6, two additional states are needed to track i_{sd} and $\omega_{\rm e}$ references, which are w_{isd} and $w_{\omega e}$, respectively. Adding those states into (18)–(20), returns the augmented system

$$\xi_1(k+1) = [A_{\zeta 1}] \begin{bmatrix} x_{1-3}(k) \\ w_{\rm isd}(k) \\ w_{\omega e}(k) \end{bmatrix} + [B_{\xi 1}]\, u_1\,(k) + \begin{bmatrix} 0 & 0 \\ 1 & 0 \\ 0 & 1 \end{bmatrix} r_1(k) \quad (22)$$

$$y_{\rm lqr1}(k) = [C_{\rm lqr1}]\,[x(k)] + [0]\, u_1\,(k)\,. \quad (23)$$

The block diagram that describes the PMSG speed and current control is shown in Fig. 7. The LQI system is compound by a typical proportional gain which feeds the states of the model ($F_{11}\ldots_{13}$) and other proportional gains that feed the integrators (F_{14}, F_{15}, F_{24}, and F_{25}). These gains are calculated through the standard LQR solution [46].

The bus voltage controller was implemented through the same LQR strategy described above, but in a separated loop. The resulting state space system for the dc-link is given by

$$\xi_2(k+1) = [A_{\zeta 2}] \begin{bmatrix} v_{\rm dc}(k) \\ w_v(k) \end{bmatrix} + [B_{\xi 2}]\, u_2\,(k) + \begin{bmatrix} 0 \\ 1 \end{bmatrix} r_2(k). \quad (24)$$

The block diagram that describes the system (24) with LQI control is shown in Fig. 8. The selection of the *Q* and *R* matrices consisted on playing with the weights of these matrices and observing the results in order to find the best combination. Along this process, it was considered that the dynamics of the loops must be distant enough for the simplifications to be valid [45]. Once defined, *Q* and *R* kept constant along all simulations runs.

IV. Simulations

In order to evaluate the relationship between the system variables and the frequency support performance in the microgrid from Fig. 2, multiple simulation runs were implemented

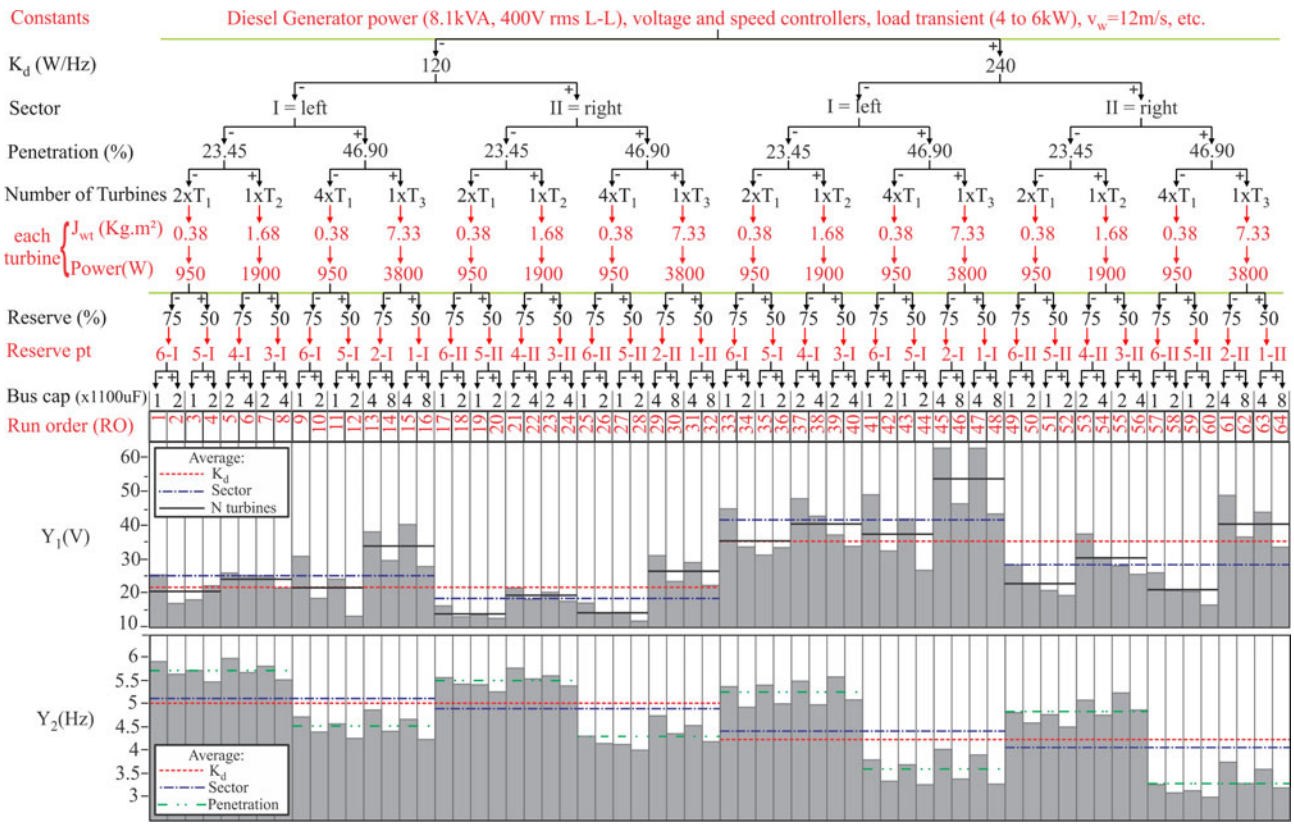

Fig. 9. Simulation structure (DOE three) and results for Y_1 and Y_2.

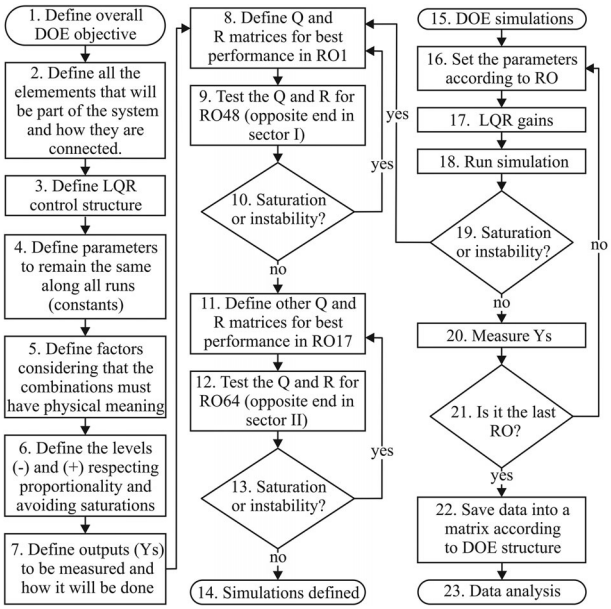

Fig. 10. Flowchart considered to define the DOE.

sweeping the variables according to the structure from Fig. 9. This structure follows a DOE concept [40], keeping some parameters constant, manipulating others and measuring the responses (Ys). The DOE structure was defined according to the flowchart from Fig. 10, following steps 1–14.

First of all, the overall objective, the system elements (see Fig. 2), and the LQR structure (see Figs. 7 and 8) have been well defined, attending to the first three steps requirements.

In step 4, the constant parameters were set. They are specified in the first row of the tree, representing the contour conditions which the effects were not evaluated in the DOE.

The manipulated parameters, also called as factors, were defined in step 5. The definition had to guarantee that all runs combinations have a physical meaning.

The first manipulated factor (K_d) represents how aggressive the GSC control is. It is simplified by a droop constant in watt per frequency deviation (W/Hz). The second factor was the operating sector of the turbines, already defined in Fig. 3. The third factor represented the wind power penetration levels in the microgrid, defined as the wind rated generation divided by the diesel generator rated power. The fourth represented the number of turbines operating in the microgrid, with the intent was to compare multiple smaller turbines versus a single bigger one. The fifth factor meant the power reserve in comparison to the nominal power, which corresponds to steady-state operating point of the turbines before the transient. The sixth was the bus capacitor value.

In step 6, the levels for each factor were set. This process was done carefully in order to avoid saturations in the system variables along the transients, as well as respect the proportionality of the DOEs [40]. It started by defining the baseline configuration for Sector I (RO1), which has $2 \times T_1$, each one with a dc-link of 1100 μF and a GSC with $K_d = 120$ W/Hz. The

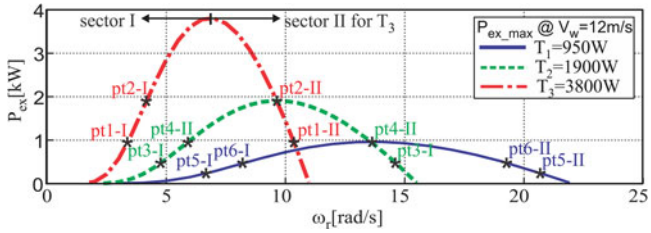

Fig. 11. Turbines power curves and initial operating points (reserve).

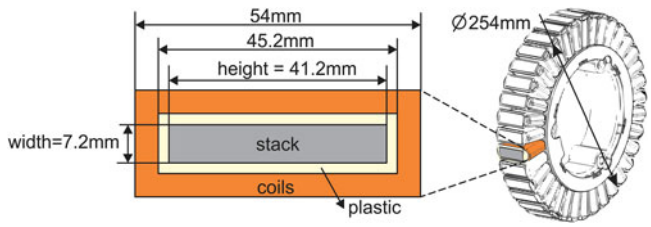

Fig. 12. Baseline machine dimensions.

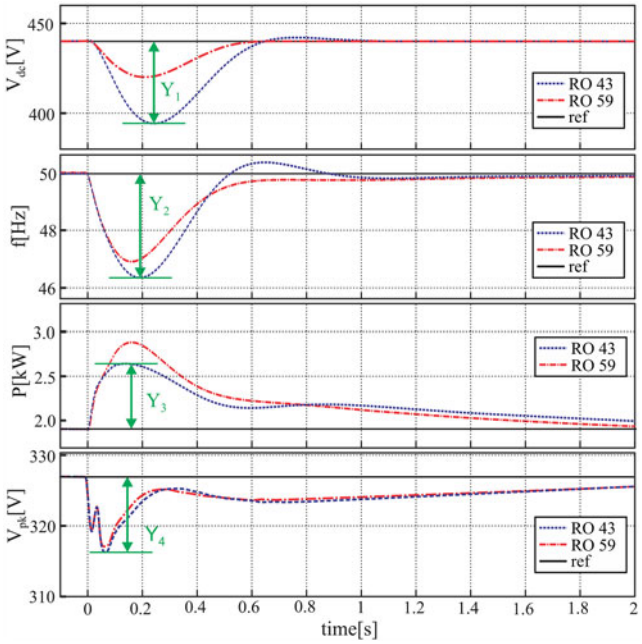

Fig. 13. Ys measurements definition exemplifyed through RO43 and 59.

turbines operate in Sector I, having a power reserve of 75%, corresponding to the pt5-I in Fig. 11. There is an equivalent configuration operating in Sector II, which starts from pt5-II and is defined as RO17. All other runs are multiple of RO1 and RO17, following the logic described above.

A preliminary saturation check can be achieved by testing the all (–) and the all (+) configurations. However, these two conditions do not always cover the rest, as some interactions could bring unexpected behaviors.

In order to respect the proportionalities, three distinct turbine were considered along the simulations, defined as T_1, T_2, and T_3, rated as 950, 1800, and 3800 W, respectively.

Each one operates in a range of speed as shown in Fig. 11, providing its own inertia constant, calculated through (6). The turbines T_2 and T_3 were derived as multiples of T_1 according to their power rating. The main assumption to obtain T_2 and T_3 parameters is that all turbines provide the same EMF at the respective nominal speeds. It implies on different K_m and K_t, which were proportionally calculated from T_1. From the derived K_m and K_t, the stack area was calculated increasing proportionally the stack height and keeping stack width constant. The number of turns was kept constant among the three machines and the wire diameter was increased in order to keep the copper losses within the same proportion as T_1. The machine radius increased proportionally to fit the new coils, not considering cost or volume optimization, which is not the intent. The baseline machine is shown in Fig. 12 and the resulting parameters for the three PMSGs are listed in Table I.

The machine chosen as the baseline (T_1) is able to generate up to 1 kW and rotate up to 40 rad/s before field-weakening region. As it was not optimized for wind applications, the machine speed range and rated power do not attend properly (5). Therefore, for studies purposes, the blades radius was chosen to be 7 m to match the speed range and the power in the output was rescaled in a 1/70 ratio to match the machine rated power. Accordingly, the baseline turbine (T_1) provides up to 950 W at $v_w = 12$ m/s.

The steady-state turbine operating points for each simulation run from Fig. 9 are highlighted in Fig. 11. These points are far from the maximum power point only in order to avoid saturation in wind power along the transient, what would affect the quantitative analysis. It is not likely that 75% would be used in an actual application.

As part of step 7, the simulations outputs (Ys) were defined as: dc-link voltage drop (Y_1) in volts; ac bus frequency drop (Y_2) in hertz; delta wind power (Y_3) in watts and ac bus voltage drop (Y_4) in volts. These values are measured under a load transient from 4 to 6 kW at a certain operation time when in steady state. As a matter of example and clarification, the Ys for RO43 and RO59 are shown in Fig. 13. The same measurement pattern has been considered along the 64 runs.

In step 8, *Q* and *R* matrices were defined for Sector I considering RO1 as baseline. From step 9 to 10, the *Q* and *R* matrices were tested for an opposite end configuration (RO48). If no instability or saturation was found, an equivalent process was run for Sector II, from steps 11 to 13. The configurations of matrices were defined with the intent to obtain the best transient response for each sector. This was a preliminary check, as some interactions could bring unexpected behaviors for other ROs.

Once the simulations are defined, the DOE was run according to steps 15–23. The stability and saturation were observed in each run. When all simulations were OK, the data were analyzed graphically and quantitatively.

Starting with a graphical analysis, the values of Y_1 and Y_2 for each run were attached to the DOE three, as shown in the lower part of Fig. 9. The averages of the main factors were highlighted to support the analysis. Considering Y_1, K_d average shows that dc-link voltage is lower for $K_d(-)$, ROs 1–32, than $K_d(+)$, ROs 33–64.

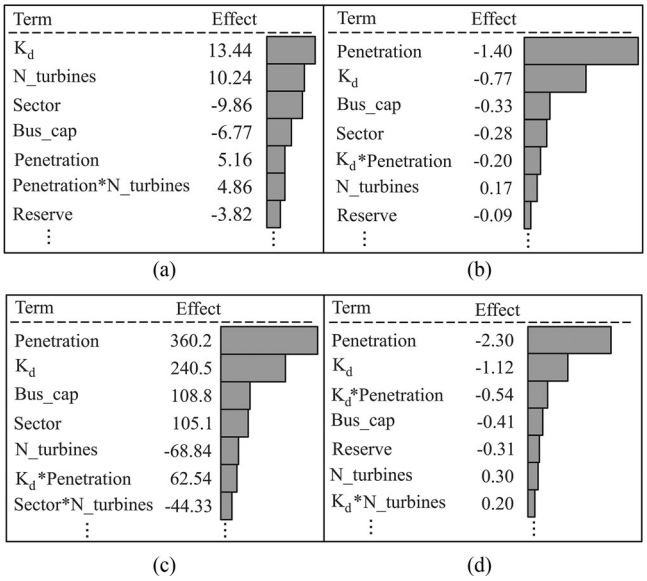

Fig. 14. Pareto plot for (a) dc-link voltage drop (Y_1), (b) ac-bus frequency drop (Y_2), and (c) delta wind power (Y_3). (d) ac-bus voltage drop (Y_4).

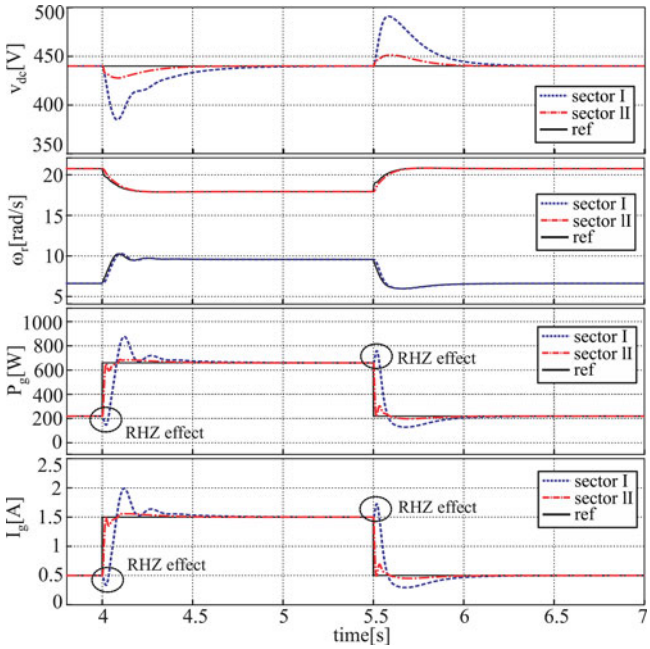

Fig. 15. DC-link regulation for Sectors I and II for load steps at $v_w = 12$ m/s.

The reason is that having a more aggressive control in the GSC, more power is drained from the dc-link, increasing the voltage drop during the transient.

The Pareto chart from Fig. 14(a) reinforces this conclusion, showing that K_d is the main factor to affect Y_1, moving the average 13.44 V upwards when going from $K_d(-)$ to $K_d(+)$.The second most important factor, N_ turbines, implies that multiple SWTs (–) provide lower voltage drop than a single bigger one (+). The sector comes as third more important factor, decreasing the average in 10.24 V by moving from Sector I (–) to Sector II (+), due to the RHZ mentioned previously. Smaller WTs provide faster dynamics, releasing the kinetic energy faster as well as working in higher speed, providing relatively higher kinetic energy than single bigger WT. The range of the results was 12.15 V (RO28) to 63.05 V (RO47).

The Pareto chart shows the effect of each factor, which is calculated by taking the average off all the runs where the factor is (+) and subtract by the average of all the runs where the factor is (–). The main factor to drive Y_2 was the penetration level, as going from 23.45% (–) to 46.90% (+) reduced the frequency drop in 1.4 Hz according to Fig. 14(b). Higher penetration provided lower drop due to frequency compensation loop in the GSC. The second factor was K_d, which decreased the drop as it became higher (+). Higher bus capacitor (+) and Sector II operation (+) decreased the frequency deviation as well. The range of the results was 3 Hz (RO60) to 6 Hz (RO5), which are quite high in general. It is a result of the low microgrid inertia, purposely designed in order to emphasize the analysis.

The Pareto chart for Y_3 is shown in Fig. 14(c). The first three factors are in the same order as Y_2, reinforcing the relationship between frequency regulation and active power. The results ranged from 159.29 W (RO7) to 1028.15 W (RO58). Regarding Y_4, the main factor was penetration, followed by K_d, interaction K_d^* penetration, Bus_cap, etc, as seen in Fig. 14(d). The range was 10.58 V (RO60) to 16.27 V (RO53).

The interaction K_d^* penetration showed up between the six most important factors for Y_2, Y_3, and Y_4. This interaction means that when K_d is low, the penetration does not affect as much as when it is high. It happens because once there is no frequency compensation ($K_d = 0$), higher penetration would provide higher transients, due to the microgrid lower inertia.

Although most factors were doubled from level (–) to level (+), sector stood out for most Ys, meaning that is an important factor to be considered when optimizing the system. In order to highlight the sector effect through waveforms, load steps were applied into two T_1 turbines operating respectively in Sectors I and II. The resulting bus voltage (v_{dc}), shaft speed (ω_r), generated power (P_g), and current (I_g) are shown in Fig. 15. It can be perceived that v_{dc} deviation in the transients is considerably lower in Sector II than in Sector I. The current i_g shows the effect of the RHZ when first goes down at $t = 4$ s for Sector II while it should go up according to the control intent.

V. Conclusion

This paper investigated the SWT frequency regulation support capability in a lower power wind-diesel isolated microgrid. Although the frequency support capability depends on more system variables, six factors were selected as the most relevant to be simulated, which are GSC droop constant value, wind penetration, number and size of turbines, turbine operating sectors in the power generation curve, power reserve and dc-link capacitor size.

The frequency deviation for a defined load step was measured dynamically considering 64 different configurations of the variables selected. The analysis was done in closed loop,

considering an optimum control technique to provide fair comparison among the variables and provide the optimum control trajectory. The gains and bandwidth were automatically set by the LQR controller for each simulation run, considering one set of Q and R matrices for Sector I and another one for Sector II. Both sets were tuned to obtain the best transient for each sector.

The simulations were organized in a DOE structure, supporting important conclusions in a clear and fast way. A flowchart explaining how the DOE structure was defined has been provided. The results (Ys) were measured in predefined methods for all 64 simulation configurations detailed in the experiment tree. The results were first shown through graphical approach, connecting the magnitudes to the respective tree configuration (RO). Analytical methods like Pareto plots were also used to compare the effect of each factor in the responses.

Both graphical and analytical analyses are in agreement with the physics-based expected behavior for each configuration. Higher droop constant (K_d) provides lower frequency deviations as it injects more active power along the transitory. The operating Sector II provides higher frequency support capability due to the kinetic energy release or absorption in favor to the control intent, supporting the dc-link better regulation. Besides, it was seen that multiple SWTs provide lower bus voltage drop and lower frequency deviation than a single bigger one. The SWTs provide faster dynamics, releasing kinetic energy quicker as well as working in higher speed, providing relatively higher kinetic energy than single bigger WT. The dc-link capacitance keeps the dc-link better regulated, allowing the GSC to inject more active power. Power reserve did not affect the results significantly.

Considering the simulations results and assuming that the objective is to decrease the frequency deviation disregarding any limitation, the system should have a high penetration with a high droop constant, bulky bus capacitors and operate in Sector II with multiple small turbines operating with a power reserve big enough to compensate the worst transients. The dc-link voltage should not go lower than a limit which would impact the GSC functionality. However, bulky bus capacitors are costly, big power reserve does not allow the wind energy to be fully used, increasing the cost of the energy. Besides, Sector II operation provides higher mechanical stresses. In the end, the system has to be optimized considering all these variables which interactions are shown in this work, including system cost, reliability, etc. This optimization or any other can be achieved using the presented methodology by following the defined flowchart or even adapting it as needed.

It is important to highlight that these absolute resulting values are related to this experiment only, with this inference space. Any different factor level set would provide different absolute results, but not relative ones, assuming no saturation inserted.

REFERENCES

[1] R. H. Lasseter and P. Paigi, "Microgrid: A conceptual solution," in *Proc. IEEE 35th Annu. Power Electron. Spec. Conf.*, vol. 6, 2004, pp. 4285–4290.

[2] R. H. Lasseter, "MicroGrids," in *Proc. IEEE Power Eng. Soc. Winter Meeting*, vol. 1, 2002, pp. 305–308.

[3] J. A. P. Lopes, C. L. Moreira, and A. G. Madureira, "Defining strategies for microgrids islanded operation," *IEEE Trans. Power Syst.*, vol. 21, no. 2, pp. 916–924, May 2006.

[4] J. M. Guerrero, J. C. Vasquez, J. Matas, L. G. de Vicuna, and M. Castilla, "Hierarchical control of droop-controlled AC and DC microgrids—A general approach toward standardization," *IEEE Trans. Ind. Electron.*, vol. 58, no. 1, pp. 158–172, Jan. 2011.

[5] I. Y. Chung, W. Liu, D. A. Cartes, E. G. Collins, and S. Moon, "Control methods of inverter-interfaced distributed generators in a microgrid system," *IEEE Trans. Ind. Appl..*, vol. 46, no. 3, pp. 1078–1088, May/ Jun. 2010.

[6] A. Banerji, S. K. Biswas, and B. Singh, "Enhancing quality of power to sensitive loads with microgrid," *IEEE Trans. Ind. Appl.*, vol. 52, no. 1, pp. 360–368, Jan./Feb. 2016.

[7] Y. A. I. Mohamed and E. F. El-Saadany, "Adaptive decentralized droop controller to preserve power sharing stability of paralleled inverters in distributed generation microgrids," *IEEE Trans. Power Electron.*, vol. 23, no. 6, pp. 2806–2816, Nov. 2008.

[8] N. Soni, S. Doolla, and M. C. Chandorkar, "Inertia design methods for islanded microgrids having static and rotating energy sources," *IEEE Trans. Ind. Appl.*, vol. 52, no. 6, pp. 5165–5174, Nov./Dec. 2016.

[9] N. Soni, S. Doolla, and M. C. Chandorkar, "Analysis of frequency transients in isolated microgrids," in *Proc. IEEE Ind. Appl. Soc. Annu. Meeting*, 2016, pp. 1–9.

[10] C. A. Hernandez-Aramburo, T. C. Green, and N. Mugniot, "Fuel consumption minimization of a microgrid," *IEEE Trans. Ind. Appl.*, vol. 41, no. 3, pp. 673–681, May/Jun. 2005.

[11] R. Maharjan, F. Guo, and R. Sharma, "Control strategy for islanded microgrid integrating renewable energy with storage and diesel generator," in *Proc. IEEE Ind. Appl. Soc. Annu. Meeting*, 2016, pp. 1–7.

[12] C. Abbey and G. Joos, "A stochastic optimization approach to rating of energy storage systems in wind-diesel isolated microgrids," *IEEE Trans. Power Syst.*, vol. 24, no. 1, pp. 418–426, Feb. 2009.

[13] Y. Sun, Z. Zhang, G. Li, and J. Lin, "Review on frequency control of power systems with wind power penetration," in *Proc. Int. Conf. Power Syst. Technol.*, 2010, pp. 1–8.

[14] P. Gopakumar and M. J. B. Reddy, "Renewable energy utilization using low power microgrid system," in *Proc. Int. Conf. Power Energy Control*, 2013, pp. 751–755.

[15] *Small Wind World Report*, World Wind Energy Assoc., Bonn, Germany, 2013.

[16] N. A. Orlando, M. Liserre, R. A. Matromauro, and A. Dell'Aquila, "A survey of control issues in PMSG-based small wind-turbine systems," *IEEE Trans. Ind. Informat.*, vol. 9, no. 3, pp. 1211–1221, Aug. 2013.

[17] P. M. Pardalos, S. Rebennack, M. V. F. Pereira, N. A. Iliadis, and V. Pappu, *Handbook of Wind Power Systems*. Berlin, Germany: Springer, 2013.

[18] *Technology Roadmap: Wind Energy*, Int. Energy Agency, Paris, France, 2013.

[19] Y. Wang, G. Delile, H. Bayem, X. Guilaud, and B. Francois, "High wind power penetration in isolated power systems—Assessment of wind inertial and primary frequency responses," *IEEE Trans. Power Syst.*, vol. 28, no. 3, pp. 2412–2420, Aug. 2013.

[20] W. Yao and K. Y. Lee, "A control configuration of wind farm for load-following and frequency support by considering the inertia issue," in *Proc. IEEE Power Energy Soc. Gen. Meeting*, 2011, pp. 1–6.

[21] Y. Sun, Z. Zhang, G. Li, and J. Lin, "Review on frequency control of power systems with wind power penetration," in *Proc. Int. Conf. Power Syst. Technol.*, 2010, pp. 1–8.

[22] L. Ruttledge, N. W. Miller, J. O"Sullivan, and D. Flynn, "Frequency response of power systems with variable speed wind turbines," *IEEE Trans. Sustain. Energy*, vol. 3, no. 4, pp. 683–691, Oct. 2012.

[23] E. Muljadi, V. Gevorgian, M. Singh, and S. Santoso, "Understanding inertial and frequency response of wind power plants," in *Proc. IEEE Power Electron. Mach. Wind Appl.*, 2012, pp. 1–8.

[24] J. M. Mauricio, A. Marano, A. Gomez-Exposito, and J. L. M. Ramos, "Frequency regulation contribution through variable-speed wind energy conversion systems," *IEEE Trans. Power Syst.*, vol. 24, no. 1, pp. 173–180, Feb. 2009.

[25] J. I. Yoo, J. Kim, and J. Park, "Converter control of PMSG wind turbine system for inertia-free stand-alone microgrid," in *Proc. IEEE Ind. Appl. Soc. Annu. Meeting*, 2016, pp. 1–8.

[26] T. Zhou and B. Francois, "Energy management and power control of a hybrid active wind generator for distributed power generation and grid integration," *IEEE Trans. Ind. Electron.*, vol. 58, no. 1, pp. 95–104, Jan. 2011.
[27] Y. Guan, J. C. Vasquez, and J. M. Guerrero, "Coordinated secondary control for balanced discharge rate of energy storage system in islanded AC microgrids," *IEEE Trans. Ind. Appl.*, vol. 52, no. 6, pp. 5019–5028, Nov./Dec. 2016.
[28] A. Tani, M. B. Camara, and B. Dakyo, "Energy management in the decentralized generation systems based on renewable energy—Ultracapacitors and battery to compensate the wind/load power fluctuations," *IEEE Trans. Ind. Appl.*, vol. 51, no. 2, pp.1817–1827, Mar./Apr. 2015.
[29] T. Lukasievicz, R. V. de Oliveira, and G. G. Dranka, "Control of an islanded wind-diesel microgrid with high penetration level of wind generation," in *Proc. IEEE Power Energy Soc. Gen. Meeting*, 2015, pp. 1–5.
[30] N. Mendis, K. M. Muttaqi, S. Perera, and M. N. Uddin, "A novel control strategy for stand-alone operation of a wind dominated RAPS system," in *Proc. IEEE Ind. Appl. Soc. Annu. Meeting*, 2011, pp. 1–8.
[31] N. A. Orlando, M. Liserre, and A. Dell'Aquila, "Management of power excess in wind turbine system," in *Proc. Eur. Conf. Power Electron. Appl.*, 2009, pp. 1–10.
[32] S. Alepuz, A. Calle, S. Busquets-Monge, S. Kouro, and B. Wu, "Use of stored energy in PMSG rotor inertia for low-voltage ride-through in back-to-back NPC converter-based wind power systems," *IEEE Trans. Ind. Electron.*, vol. 60, no. 5, pp. 1787–1796, May 2013.
[33] Y. Li, Z. Xu, and K. P. Wong, "Advanced control strategies of PMSG-based wind turbines for system inertia support," *IEEE Trans. Power Syst.*, vol. 32, no. 4, pp. 3027–3037, Jul. 2017.
[34] N. A. Orlando, M. Liserre, R. A. Mastromauro, and A. Dell'Aquila, "A survey of control issues in PMSG-based small wind-turbines systems," *IEEE Trans. Ind. Informat.*, vol. 9, no. 3, pp. 1211–1221, Aug. 2013.
[35] H. Geng, G. Yang, D. Xu, and B. Wu, "Unified power control for PMSG-based WECS operating under different grid conditions," *IEEE Trans. Energy Convers.*, vol. 26, no. 3, pp. 822–830, Sep. 2011.
[36] Y. Wang, J. Meng, X. Zhang, and L. Xu, "Control of PMSG-based wind turbines for system inertial response and power oscillation damping," *IEEE Trans. Sustain. Energy*, vol. 6, no. 2, pp. 565–574, Apr. 2015.
[37] Y. Wang, G. Delille, H. Bayern, X. Guillaud, and B. Francois, "High wind power penetration in isolated power system—Assessment of wind inertial and primary frequency responses," *IEEE Trans. Power Syst.*, vol. 28, no. 3, pp. 2412–2420, Aug. 2013.
[38] Y. Tan, K. M. Muttaqi, P. Ciufo, and L. Meegahapola, "Enhanced frequency response strategy for a PMSG-based wind energy conversion system using ultracapacitor in remote area power supply systems," *IEEE Trans. Ind. Appl.*, vol. 53, no. 1, pp. 549–558, Jan./Feb. 2017.
[39] X. Yuan, F. Wang, R. Burgos, Y. Li, and D. Boroyevich, "DC_link voltage control of full power converter for wind generator operating in weak grid systems," *IEEE Trans. Power Electron*, vol. 24, no. 9, pp. 2178–2192, Sep. 2009.
[40] R. L. Mason, R. F. Gunst, and J. L. Hess, *Statistical Design and Analysis of Experiments: With Applications to Engineering and Science*, 2nd ed. Hoboken, NJ, USA: Wiley, 2003.
[41] A. Rolan, A. Luna, G. Vasquez, D. Aguiar, and G. Azevedo, "Modeling of a variable speed wind turbine with a permanent magnet synchronous generator," in *Proc. IEEE Symp. Ind. Electron.*, 2009, pp. 734–739.
[42] P. Tielens, S. de Rijcke, K. Srivastava, M. Reza, A. Marinopoulos, and J. Driesen, "Frequency support by wind power plants in isolated grids with varying generation mix," in *Proc. IEEE Power Energy Soc. Gen. Meeting*, 2012, pp. 1–8.
[43] T. A. Lipo and D. W. Novotny, *Vector Control and Dynamics of AC Drivers*. London, U.K.: Oxford Univ. Press, 1996.
[44] X. Zeng, Z. Chen, and F. Blaabjerg, "Design and comparison of full-size converters for large variable-speed wind turbines," in *Proc. Eur. Conf. Power Electron. Appl.*, 2007, pp. 1–10.
[45] R. Engleitner, A. Nied, M. S. M. Cavalca, and J. P. da Costa, "Small wind turbines operating points and their effect on the DC-link control for frequency support on low power microgrids with high wind penetration," in *Proc. IEEE Int. Conf. Ind. Appl.*, 2016, pp. 1–8.
[46] D. E. Kirk, *Optimal Control Theory: An Introduction*. Englewood Cliffs, NJ, USA: Prentice-Hall, 1970.
[47] *Wind Turbines Design Requirements*, IEC 61400-1, 2005(E).

Raffael Engleitner was born in Giruá, Brazil, in 1986. He received the B.S. and master's degrees in electrical engineering from the Federal University of Santa Maria, Santa Maria, RS, Brazil, in 2009 and 2011, respectively. He is currently working toward the Ph.D. degree with the State University of Santa Catarina, Joinville, SC, Brazil.

His researches interests include modeling and control of power converters, electrical machines, and smart grids.

Ademir Nied (S'03–M'08) received the B.E. degree in electrical engineering from the Federal University of Santa Maria, Santa Maria, RS, Brazil, in 1987; the M.S. degree in industrial informatics from the Federal Technological University of Parana, Pato Branco, PR, Brazil, in 1995; and the Ph.D. degree in electrical engineering from the Federal University of Minas Gerais, Belo Horizonte, MG, Brazil, in 2007.

Since 1996, he has been an Associate Professor with the Department of Electrical Engineering, State University of Santa Catarina, Joinville, SC, Brazil. From 2015 to 2016, he was a Visiting Professor with the Wisconsin Electric Machines and Power Electronics Consortium, University of Wisconsin–Madison, Madison, WI, USA. His research interests include electrical machines, control of electrical drives, and renewable energy.

Mariana Santos Matos Cavalca was born in São José dos Campos, SP, Brazil, in 1984. She received the master's and doctor degrees in electronic and computing engineering from the Technological Institute of Aeronautics, São José dos Campos, in 2008 and 2011, respectively.

She was a Control and Automation Engineer in 2007. She is currently the Postgraduation Electrical Engineering Program Coordinator with the State University of Santa Catarina, Joinville, SC, Brazil. Her areas of interest are predictive control, fault-tolerant control, and optimal control.

Jean Patric da Costa was born in Santa Maria, Brazil, in 1979. He received the B.S., master's, and Ph.D. degrees in electrical engineering from the Federal University of Santa Maria (UFSM), in 2004, 2006, and 2010, respectively.

He is currently a Professor with the Department of Electrical Engineering, Federal University of Technology - Paraná (UTFPR). His research interests include control of static converters, smart grids, ancillary services, and distribution networks with distributed generators.